

Pump-triple sum-frequency-probe spectroscopy of transition metal dichalcogenides

Darien J. Morrow, Daniel D. Kohler, Yuzhou Zhao, Song Jin, and John C. Wright*

*Department of Chemistry, University of Wisconsin–Madison,
1101 University Ave, Madison, WI 53706, United States*

(Dated: September 17, 2019)

Triple sum-frequency (TSF) spectroscopy measures multidimensional spectra by resonantly exciting multiple quantum coherences of vibrational and electronic states. In this work we demonstrate pump-TSF-probe spectroscopy in which a pump excites a sample and some time later three additional electric fields generate a probe field which is measured. We demonstrate pump-TSF-probe spectroscopy on polycrystalline, smooth, thin films and spiral nanostructures of both MoS₂ and WS₂. The pump-TSF-probe spectra are qualitatively similar to the more conventional transient-reflectance spectra. While transient-reflectance sensitivity suffers under low surface coverage, pump-TSF-probe sensitivity is independent of the sample coverage and nanostructure morphologies. Our results demonstrate that pump-TSF-probe is a valuable methodology for studying microscopic material systems.

I. INTRODUCTION

Pump-probe spectroscopy is a ubiquitous methodology for investigating the dynamics and energetics of excited systems on sub-picosecond time scales. In a pump-probe experiment, a pump excites the system of interest and a probe interrogates the evolved system at a later time, T . The differences in the probe signal with and without the pump inform on system evolution. Most merits of a pump-probe experiment, such as sensitivity and selectivity, are determined by the choice of a specific probe methodology, of which there are many.[1–10] The development of Coherent Multidimensional Spectroscopy (CMDS) offers promising possibilities for new probes because CMDS methods can have increased selectivity compared to conventional methods.[11–17] CMDS uses multiple optical interactions to create a multiple quantum coherence within the material whose optical emission is measured. The ability/requirement to couple multiple quantum states together leads to the selectivity inherent within CMDS. By preceding a CMDS pulse sequence by a pump, the selectivity of CMDS can be leveraged as a probe in a “pump-CMDS-probe” measurement.[2, 3, 6, 18, 19] In this paper we introduce triple sum-frequency (TSF) spectroscopy as a new probe for material systems by measuring the pump-induced TSF response of model semiconductor systems: transition metal dichalcogenides (TMDCs).

TSF spectroscopy uses three tunable electric fields, E_1 , E_2 , and E_3 to create coherences at increasingly higher energies. These coherences cooperatively emit a new electric field with frequency $\omega_{\text{out}} = \omega_1 + \omega_2 + \omega_3$ in a direction defined by phase-matching. Scanning the multiple driving laser frequencies enables collection of a multidimensional spectrum whose cross-peaks identify dipole coupling among probed states. The selectivity of TSF is due to the increase in output intensity

achieved when the driving fields are resonant with multiple states; the multiple resonance conditions act as a “fingerprint”.[20] TSF has been used to investigate vibrational and electronic coupling in molecules,[21–26] and recently, TSF has revealed the electronic states of MoS₂ and the mixed-vibrational-electronic coupling of organic-inorganic perovskites.[27, 28]

In this paper, we measure the pump-TSF-probe response of MoS₂ and WS₂, which are layered semiconductors in the TMDC family.[29] The bandedge optical spectrum of MoS₂ is dominated by two features labeled A ($\hbar\omega_A \approx 1.8$ eV) and B ($\hbar\omega_B \approx 1.95$ eV) which originate from high binding energy excitonic transitions between spin-orbit split bands (see absorption spectrum and inset diagram in Figure 1).[30–35] Likewise, the optical response of WS₂ is dominated near the bandedge by the A feature ($\hbar\omega_A \approx 2$ eV). The present work expands upon our previous work on the unpumped TSF response of MoS₂,[27] the extensive body of harmonic generation work on TMDCs (c.f. the review by Autere *et al.* [36] and references therein), and the innovative pump-second-harmonic-generation probe work accomplished on semiconductors.[37–44]

In our previous work on the unpumped TSF response of MoS₂ we noted important differences between the nonlinear TSF probe and conventional linear probes, such as absorption or reflection.[27] The intensity of homodyne detected TSF has transition dipole scaling of μ^8 and state density scaling of J^2 . This scaling is in contrast to self-heterodyne detected absorption and reflection measurements which scale as μ^2 and J . The steep scaling of TSF with transition dipole compared to state density can depress substrate effects which dominate reflection measurements. For instance, we have found that in the case of large transition dipole excitonic transitions, TSF only measures photons which originated in a single nanostructure whereas reflection measurements sense reflections from both the nanostructure and reflections from the substrate. Likewise, the dipole scaling of other CMDS techniques has enabled the measurement of protein structure against large backgrounds when conventional absorption

* wright@chem.wisc.edu

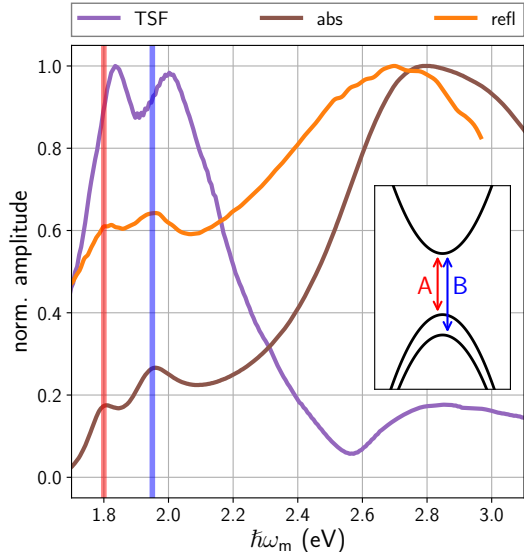


FIG. 1. Normalized amplitude 1D spectra of MoS₂ thin films. The absorption measurement was originally shown in Czech *et al.* [45]. The TSF and reflection contrast measurements were originally shown in Morrow *et al.* [27]. Vertical bars are guides to the eyes set at 1.80 and 1.95 eV. The inset is a cartoon of the band structure of MoS₂ at the *K* point. Only the valence bands are shown as spin-orbit-split because the splitting of the conduction bands is generally too small to be observed for MoS₂.

measurements fail.[46, 47] The ability of TSF to selectively interact with large dipole transitions is highlighted in Figure 1 for the example of MoS₂. The absorption and reflection spectra of the MoS₂ thin film are dominated by higher energy transitions with large joint density of states and low transition moments. Conversely, the TSF spectrum (in this case $\omega_1 = \omega_2 = \omega_3 = \omega_{\text{out}}/3$, a third harmonic generation, THG, spectra) is dominated by the large transition dipole A and B excitonic transitions.

The structure of the rest of this paper is as follows: In the Theory section we describe how to calculate transient-TSF response and graphically compare it to the response from other common spectroscopies. In the Experimental section we describe our spectrometer and our samples. In the Results section we present our transient-TSF measurements on TMDCs. We first examine how the multidimensional TSF spectrum is affected by an optical pump. We find that the multidimensional TSF spectrum can be fully described by the one-dimensional pump-THG-probe spectrum. We then compare pump-THG-probe to pump-reflectance-probe spectroscopy; we demonstrate that although their lineshapes appear slightly different, the same pump-induced physics can explain both spectra. Finally we demonstrate the utility of transient-TSF for measuring TMDC nanostructures. We finish the paper by discussing how transient-

TSF might be used in the future on other systems.

II. THEORY

A. The linear and non-linear probe

In this section we present the correspondence between the reflectance and TSF of a material. We investigate the phenomenological, microscopic properties that are responsible for the susceptibility and also how the susceptibility dictates the electric field output. Readers interested in first-principle calculations of TMDC nonlinear susceptibility should consult refs.[48–52]. Our analysis uses standard perturbation theory.[53, 54] The material polarization, P , is expanded in orders of the electric field, E :

$$P = \epsilon_0 \left(\chi^{(1)} E + \chi^{(2)} E^2 + \chi^{(3)} E^3 + \dots \right), \quad (1)$$

where $\chi^{(n)}$ is the n^{th} -order susceptibility and ϵ_0 is the permittivity of free space. The linear susceptibility, $\chi^{(1)}$, determines the response of linear spectroscopies such as absorption and reflection. The third-order susceptibility, $\chi^{(3)}$, determines the response of non-linear spectroscopies such as TSF.

Within the dipole approximation, $\chi^{(1)}$ is constructed from a sum over all initial and final states:

$$\chi^{(1)}(\omega_1) = \sum_{a,g} \frac{\mu_{ag}^2}{\Delta_{ag}^1}, \quad (2)$$

where $\Delta_{ag}^1 \equiv \omega_{ag} - \omega_1 - i\Gamma$, μ_{ag} and ω_{ag} are the transition dipole and frequency difference between states a and g , Γ is a damping rate which accounts for the finite width of the optical transitions, and ω_1 is the driving frequency. We see from Equation 2 that when the driving field is resonant ($\omega_1 = \omega_{ag}$), $\chi^{(1)}$ is large and the interaction with light is strong.

Like Equation 2, the TSF susceptibility is a sum over states, but we must consider three sequential excitations $g \rightarrow a \rightarrow b \rightarrow c$:

$$\chi^{(3)}(-\omega_{321}, \omega_1, \omega_2, \omega_3) = \mathcal{P} \sum_{c,b,a,g} \frac{\mu_{gc}\mu_{cb}\mu_{ba}\mu_{ag}}{\Delta_{gc}^{123}\Delta_{gb}^{12}\Delta_{ga}^1}, \quad (3)$$

$$\begin{aligned} \Delta_{ga}^1 &\equiv \omega_{ag} - \omega_1 - i\Gamma, \\ \Delta_{gb}^{12} &\equiv \omega_{bg} - \omega_{21} - i\Gamma, \\ \Delta_{gc}^{123} &\equiv \omega_{cg} - \omega_{321} - i\Gamma, \\ \omega_{21} &\equiv \omega_2 + \omega_1, \\ \omega_{321} &\equiv \omega_3 + \omega_2 + \omega_1, \end{aligned}$$

where \mathcal{P} is a permutation operator which accounts for all combinations of field-matter interactions. If only the triple sum transition is resonant, we can approximate all other resonance (Δ) terms as constant and arrive at an

expression similar to Equation 2:[27]

$$\chi^{(3)}(\omega_{123}) \propto \sum_{a,g} \frac{\mu_{ag}^4}{\Delta_{ag}^{123}}. \quad (4)$$

We now consider how the linear and third-order susceptibilities dictate the reflectance and TSF response, respectively. Both relations are formulated using Maxwell's equations via continuity relations (boundary conditions) between the incident, reflected, and transmitted fields. For ease of comparison, we will analyze the simple limit of an extremely thin film (thickness much less than the wavelength of light) on a transparent substrate. We also restrict consideration to normal incidence. Including thickness and angular dependence is straightforward but needlessly complex for our intent of illustrating qualitative differences between methodologies. These conditions are reasonable for many of the samples and experiments we consider here.

With these conditions, the reflectance, R , is given by[55, 56]

$$R \equiv \frac{I_{\text{reflected}}}{I_1} = \frac{(1 - A)^2 + B^2}{(1 + A)^2 + B^2}, \quad (5)$$

where

$$A \equiv n_s + \frac{\omega_1 \ell}{c} \text{Im} [\chi^{(1)}], \quad (6)$$

$$B \equiv \frac{\omega_1 \ell}{c} \text{Re} [\chi^{(1)}], \quad (7)$$

in which ℓ is the film thickness (propagation length), n_s is the substrate refractive index, c is the speed of light in vacuum, and I_j is the intensity of the j^{th} electric field. Note that when $\frac{\omega_1 \ell}{c} |\chi^{(1)}| \ll n_s$, Equation 5 is primarily determined by the substrate refractive index (large background reflectance). For example, taking a nominal $\chi^{(1)}$ value of ~ 1 , and a few-layer thickness, $\ell \sim 10$ nm, we calculate $\frac{\omega_1 \ell}{c} |\chi^{(1)}| \approx 0.1$ while $n_s \approx 1.45$ (both for excitation colors near the band edge of TMDCs), so the thin film limit will be appropriate for several samples considered in this work.

Expanding Equation 5 and keeping only terms linear in $\chi^{(1)}$, shows that the imaginary component of the thin film susceptibility is responsible for contrast from the substrate background:

$$R \approx \frac{(1 - n_s)^2 + 2(n_s - 1) \frac{\omega_1 \ell}{c} \text{Im} [\chi^{(1)}]}{(1 + n_s)^2 + 2(1 + n_s) \frac{\omega_1 \ell}{c} \text{Im} [\chi^{(1)}]}. \quad (8)$$

Equation 8 can be further simplified by Taylor expansion around $\frac{2\omega_1 \ell}{c} \text{Im} [\chi^{(1)}] = 0$:

$$R \approx R_0 - \left(\frac{R_0}{1 + n_s} + \frac{1 - n_s}{(1 + n_s)^2} \right) \frac{2\omega_1 \ell}{c} \text{Im} [\chi^{(1)}], \quad (9)$$

where $R_0 \equiv \frac{(1 - n_s)^2}{(1 + n_s)^2}$ is the reflectance of the substrate-air interface.

TSF emission, or non-linear frequency conversion in general, is qualitatively different from reflectance (or transmittance) because the TSF wave originates from inside the thin film.[57] This difference brings two important consequences to the measured beam: (1) TSF emission is dark in regions where the thin film is not present, and (2) the continuity relations are acutely sensitive to the thin film non-linear polarization, rather than an incident field.[58] For the aforementioned thin film conditions, the TSF output intensity satisfies the proportionality

$$\frac{I_{\text{TSF}}}{I_1 I_2 I_3} \propto |\chi^{(3)}|^2 (\omega \ell)^2. \quad (10)$$

Unlike reflectance, thin film TSF emission obeys the same $\chi^{(3)}$ scaling as the thick film emission case,[22] where the film thickness is larger than or close to the wavelength of light, but phase mismatch effects are still small.

B. Pump-TSF-probe and TR spectroscopy

We now consider how the different nature of the reflectance and TSF probe result in different, yet similar, pump-probe measurements. For both linear and non-linear probes, we can describe the pump-induced susceptibility as a perturbation to the unpumped susceptibility:

$$\chi_{\text{pumped}}^{(n)} = \chi_{\text{unpumped}}^{(n)} + d\chi^{(n)}, \quad (11)$$

where $d\chi^{(n)} = \chi^{(n+2)} I_{\text{pump}}$ is the small pump-induced perturbation. Pump-probe methodologies often look at relative changes in the probe:

$$\text{signal metric} = \frac{X_{\text{pumped}} - X_{\text{unpumped}}}{X_{\text{unpumped}}} \quad (12)$$

in which X is the probed quantity. This normalization generally allows for electric fields which are not spectrally flat to be used as a probe.

Using reflectance as our probe (Equation 9) gives a transient response of

$$\frac{\Delta R}{R} \approx \frac{-1}{R} \left(\frac{R_0}{1 + n_s} + \frac{1 - n_s}{(1 + n_s)^2} \right) \frac{2\omega_1 \ell}{c} \text{Im} [d\chi^{(1)}]. \quad (13)$$

This expression shows that our signal metric scales as $\text{Im} [d\chi^{(1)}]$ which is the same as transient transmittance in a bulk sample (see Appendix B for a derivation). In other words, in the extremely thin film limit, transient reflectance will have lineshapes which are intuitive to those who are used to interpreting bulk transient transmittance (absorption) measurements. The intuitive correspondence between transient reflectance and transient transmittance spectroscopies will break down as $\frac{\omega_1 \ell}{c} |\chi^{(1)}|$ increases—thick samples require a full Fresnel analysis to understand the transient reflectance lineshapes.

With TSF intensity as our probe, we use Equation 11 and Equation 10 to arrive at

$$\frac{\Delta I_{\text{TSF}}}{I_{\text{TSF}}} = \frac{|\text{d}\chi^{(3)}|^2 + 2|\text{d}\chi^{(3)}||\chi^{(3)}|\cos(\text{d}\theta)}{|\chi^{(3)}|^2}, \quad (14)$$

where we have used phasor representations of the susceptibilities: $\chi^{(3)} \equiv |\chi^{(3)}|e^{i\theta}$ and $\text{d}\chi^{(3)} \equiv |\text{d}\chi^{(3)}|e^{i(\theta+\text{d}\theta)}$, in which θ can be dependent on probe frequency. If $|\text{d}\chi^{(3)}| \ll |\chi^{(3)}\cos(\text{d}\theta)|$ we can write

$$\frac{\Delta I_{\text{TSF}}}{I_{\text{TSF}}} \approx 2 \left| \frac{\text{d}\chi^{(3)}}{\chi^{(3)}} \right| \cos(\text{d}\theta), \quad (15)$$

If the pump changes only the amplitude of $\chi^{(3)}$ ($\text{d}\theta = 0, \pi$), the relative change in TSF intensity tracks the relative change in susceptibility. However, if the pump also changes the phase, the amplitude changes can be suppressed. Note that in the case of a $\pi/2$ phase shift, our assumption behind Equation 15 is invalid. It is important, then, to understand when $\text{d}\theta$ can be large. In general, θ changes rapidly near resonances; if pump induced changes shift or broaden a resonance to an extent similar to its linewidth, $\text{d}\theta$ will strongly influence the pump-TSF-probe spectrum. In the absence of dramatic resonance changes, lineshapes will closely approximate $\text{d}\chi^{(3)}/\chi^{(3)}$.

To anticipate the spectra of each technique, it is useful to consider the case of a single Lorentzian resonance perturbed by the pump. For small perturbations we can construct $\text{d}\chi^{(n)}$ using the total derivative

$$\text{d}\chi^{(n)} = \frac{\partial \chi^{(n)}}{\partial \mu} \text{d}\mu + \frac{\partial \chi^{(n)}}{\partial \omega_{ag}} \text{d}\omega_{ag} + \frac{\partial \chi^{(n)}}{\partial \Gamma} \text{d}\Gamma. \quad (16)$$

In the appendices we derive analytical expressions for the lineshapes expected from transient-TSF and transient-transmittance spectroscopies in this single resonance limit. Numerically calculated spectra are shown in Figure 2 for three different types of perturbations:

- An increase in the transition dipole, $\text{d}\mu > 0$. For an excitonic transition, state-filling and Coulomb-screening will usually lead to a decrease in the transition dipole. Note that changes in state density will cause the same lineshape as transition dipole changes.
- An increase in the resonance frequency, $\text{d}\omega_{ag} > 0$. For an excitonic transition, bandgap renormalization or Coulomb-screening can lead to decreases or increases in the resonance frequency.
- An increase in the dephasing rate, $\text{d}\Gamma > 0$. An increase in particle-particle scattering rates due to pump-excited carriers can cause the dephasing rate of a transition to increase.

The transient-reflectance spectra (see Figure 2a) are easily interpreted because changes in $\text{Im}[\chi^{(1)}]$ correlate with changes in absorptive cross-section (Equation 9). Interpretation of $\Delta R/R$ line shapes mirrors the traditional interpretation of differential transmission, $\Delta T/T$,

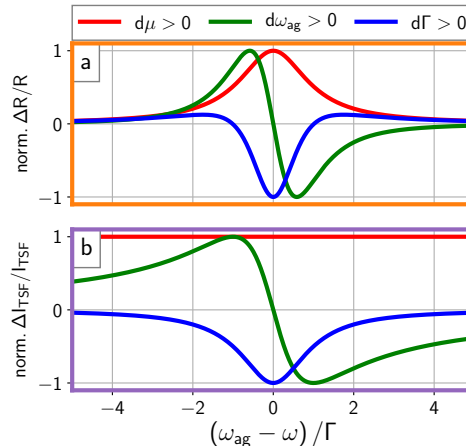


FIG. 2. Calculated transient lineshapes for a single, complex Lorentzian resonance (c.f. Equation 2 and Equation 4). (a) the transient-reflectance spectrum. (b) the transient-TSF spectrum. The spectra are produced by perturbing μ , ω_{ag} , or Γ by a factor of 10^{-5} .

for bulk samples obeying Beer's law. Increasing the dipole strength (red line) increases reflectance (positive $\Delta R/R$), with a line shape mirroring the unpumped transition. Resonance red-shifts (green line) increase reflectance to the red and decrease reflectance to the blue. Line shape broadening (blue line) decreases reflectance in the center of the resonance but increases reflectance on the wings.

The transient-TSF lineshapes (Figure 2b) have similar interpretations. Increases in transition dipole (red line) increases TSF (positive $\Delta I/I$). Unlike reflectance, the increase results in a constant $\Delta I/I$ offset. This is because the unpumped I_{TSF} lineshape has no background from substrate and so its lineshape is sharply peaked and matches that of ΔI . Line shape broadening (blue line) and blue-shifting (green line) again mirror the behavior of $-\Delta T/T$, but the $\Delta I/I$ line shapes are noticeably broader than $\Delta R/R$. Since TSF is sensitive not only to imaginary component, but also the dispersive real component of $\chi^{(3)}$ (Equation 15), the resulting lineshapes are intrinsically broader. In general, for the same dephasing rate, the transient-TSF lineshapes are broader than the transient-transmittance and transient-reflectance lineshapes.

III. EXPERIMENTAL

A. Ultrafast measurements

Our experimental setup uses an ultrafast oscillator seeding a regenerative amplifier (Spectra-Physics Tsunami and Spitfire Pro, respectively) to produce ~ 35

fs pulses centered at 1.55 eV at a 1 kHz repetition rate. The amplifier output separates into three arms. Not all arms are used in every experiment. Two arms are optical parametric amplifiers (Light-Conversion TOPAS-C) which create tunable pulses of light from ~ 0.5 to ~ 2.1 eV with spectral width on the amplitude level of FWHM ≈ 46 meV, absorptive filters and wire grid polarizers are used to isolate light of the desired color.[59] The third arm frequency doubles the output of the amplifier to create pulses centered at 3.1 eV in a β -barium-borate crystal. Each arm has its own mechanical delay stage and optical chopper. All pulses are then focused onto the sample with a 1 m focal length spherical mirror. The spatially coherent output (either the reflected probe or the triple sum of the probe) is isolated with an aperture in the reflected direction (sometimes referred to as an *epi* experiment), focused into a monochromator (Horiba Micro-HR) and detected with a thermoelectrically cooled photomultiplier tube (RCA C31034A). A dual-chopping routine is used to isolate the desired differential signal.[60] The color-dependent time-of-flight for each arm is corrected by offsetting the mechanical delay stages for each combination of pump and probe colors. We use a reflective geometry for our TSF measurements in order to minimize phase-mismatch effects.[61, 62] Unless otherwise noted, the pump fluence in these measurements is $\sim 100 \mu\text{J}/\text{cm}^2$. The visible probe beam for the reflectance-probe experiments has a fluence of $\sim 2 \mu\text{J}/\text{cm}^2$ while the NIR probe lasers for the TSF-probe experiments have a fluence of $\sim 1000 \mu\text{J}/\text{cm}^2$. All beams are hundreds of microns wide at the sample. All raw data, workup scripts, and simulation scripts used in the creation of this work are permissively licensed and publicly available for reuse.[63] Our acquisition[64] and workup[65] software are built on top of the open source, publicly available Scientific Python ecosystem.[66–68]

B. Sample preparation and characterization

Polycrystalline MoS₂ (WS₂) films were prepared by first e-beam evaporating 2 nm of Mo (W) onto a fused silica substrate and subsequent sulfidation in a tube furnace at 750 °C for 10 (30) minutes.[45] Note that this exact MoS₂ thin film sample was previously explored in Morrow *et al.* [27]. Following the methods detailed in Zhao and Jin [69], WS₂ (MoS₂) nanostructure samples on 300 nm SiO₂/Si substrates were prepared using water vapor assisted chemical vapor transport growth by heating 100 mg WS₂ (MoS₂) powder to 1200 °C at 800 torr in a tube furnace in which water vapor was produced by heating 1 g CaSO₄·2H₂O powder to 150 °C (120 °C) using heating tape wrapped around the tube furnace. 100 sccm argon was used as the carrier gas during the reaction.

Figure 3 shows optical microscope (Olympus BX51M) images, atomic force microscope (Agilent 5500) data, and Raman spectra (LabRAM Aramis, Confocal Raman/PL

Microscope, 2.33 eV excitation) of the samples. The Raman spectra show the common E_{2g}¹ and A_{1g} modes seen in WS₂ and MoS₂ at the frequencies expected for many-layer to bulk morphologies.[70–72] The polycrystalline thin films (~ 10 nm thick) are continuous, flat, and smooth samples that are much larger than the spot size of our lasers (see Figure 3a). Each MoS₂ nanostructure (Figure 3b) is a few microns wide and sparsely scattered across the substrate. The nanostructures exhibit a wide range of morphologies from screw-dislocation spirals to stacked plates. The WS₂ nanostructure (Figure 3c and d) is a single screw-dislocation spiral which is 84 nm (~ 120 layers) thick and $\sim 150 \mu\text{m}$ wide. TMDC screw-dislocation spirals are known to have excellent optical harmonic generation abilities.[73–76] Note that the perceived colors of the nanostructures in Figure 3b and Figure 3c are due to thin-film interference effects from the combination of the pyramid nanostructures, which have a large change in height across the structure, and the SiO₂/Si substrates; this class of effects have previously been explored for monolayers and nanostructures.[77–79]

IV. RESULTS AND DISCUSSION

A. MoS₂ thin film: transient-TSF

We first examine the effect of a pump on the multidimensional TSF spectrum, in which ω_1 and ω_2 are independently scanned. The output frequency of the TSF probe, $\omega_m = \omega_1 + 2\omega_2$, covers the range of the A and B excitons (1.65 - 2.25 eV). We explore this dependence with a MoS₂ thin film. In this film, the unpumped multidimensional spectra exhibit singly resonant features that depend only on the output triple sum frequency (e.g. Equation 4).[27] There are no cross peaks in the unpumped TSF spectrum because MoS₂ A and B excitons do not have the correct symmetry for our excitation beams to couple together. Like the unpumped spectrum, we found that the pump-TSF-probe spectra depends only on the triple sum frequency, regardless of pump-probe delay time. Pump-TSF-probe spectra of the MoS₂ thin film at two different delays are shown in Figure 4 ($\hbar\omega_{\text{pump}} = 3.1$ eV). At both delay times, all features run along lines of constant output color (slope of $-1/2$). We explored the multidimensional probe spectra at other frequency and T combinations (output energies up to 3 eV and population times up to 100 ps); all features found are defined solely by the output color.

Given the similarities in band structure, we expect this result to be general to all TMDCs. The simplicity of the TSF and pump-TSF-probe spectra motivate the use of Equation 4 and its associated pump-THG-probe analysis which was discussed in the Theory section. Since the output color seems to uniquely determine the observed spectra, we restrict ourselves to the case $\omega_1 = \omega_2 = \omega_m/3$ (pump-THG-probe) for the rest of this work. We will understand the lineshapes present in Figure 4 by under-

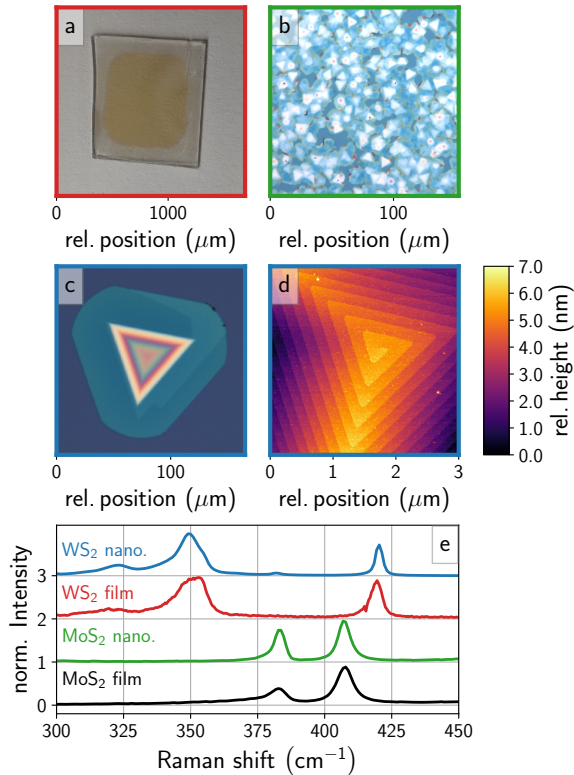


FIG. 3. TMDC Sample characterization. (a) a photograph of the WS₂ film explored in this work. (b) an optical microscope image of the MoS₂ nanostructures explored in this work. (c) optical microscope and (d) atomic force microscope image of the WS₂ nanostructure explored in this work. (e) Raman spectra of each sample; the maximum of each Raman spectrum is normalized to 1 and then offset for ease of comparison.

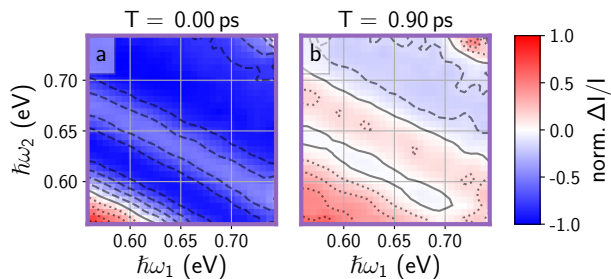


FIG. 4. Pump-TSF-probe spectra of an MoS₂ thin film at 0 ps (a) and 0.90 ps (b) delay between pump and probe interactions. In both frames $\hbar\omega_{\text{pump}} = 3.1$ eV with a fluence of $120 \mu\text{J}/\text{cm}^2$, $\omega_m = \omega_1 + 2\omega_2$, and $\vec{k}_{\text{out}} = -(\vec{k}_1 + 2\vec{k}_2)$.

standing the lineshapes of the pump-THG-probe spectroscopy presented in the next section.

B. MoS₂ thin film: transient-THG and transient-reflectance

Figure 5 shows both the pump-reflectance-probe (left) and the pump-TSF-probe (right) response of the MoS₂ thin film with pump excitation at the B exciton. Note that horizontal $3\omega_1$ slices through Figure 5b are almost equivalent to the diagonal, $\omega_1 = \omega_2$ slices of Figure 4; they differ only in the use of different pump colors. The TR and pump-THG-probe spectra are qualitatively similar. Our analysis in the Theory section indicates that phenomena like shifting and broadening will lead to similar lineshapes between the two spectroscopies while state density and dipole decreases will look different between the two spectroscopies—so our observed response is likely due to shifting and broadening of the underlying excitonic resonances. In both spectra, the measured intensity at the A and B excitons decreases when the pump is on ($\Delta I/I < 0$). The intensity decreases dominate at $T = 0$, then decay over ~ 500 fs to form spectra that undulate between positive and negative values. These undulating spectra persist for several picoseconds (data not shown).

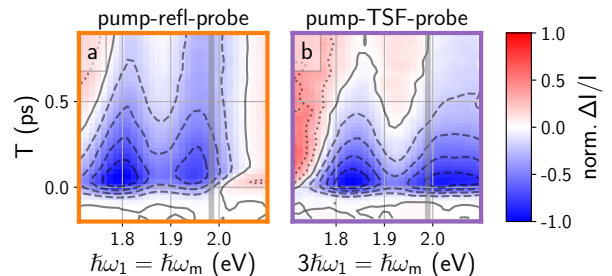


FIG. 5. Comparison of transient-reflectance spectroscopy (a) to transient-TSF spectroscopy (b) for a MoS₂ thin film. In both frames $\hbar\omega_{\text{pump}} = 1.98$ eV, as indicated by the vertical gray line. Each plot has its own colormap extent, red (dotted contours) signifies $\Delta I/I > 0$, white (solid contour) signifies $\Delta I/I = 0$, and blue (dashed contours) signifies $\Delta I/I < 0$.

The minima of the transient-THG spectrum are blue-shifted relative to the corresponding minima observed in the transient-reflectance spectrum, but roughly agree with the peak positions of the unpumped THG spectrum (Figure 1). The A and B peaks of the unpumped THG spectrum are blue-shifted by ~ 50 meV compared to the absorption/reflection spectrum. We cannot explain why the maxima of the THG and absorption/reflection spectra are different by ~ 50 meV, but we note that Wang *et al.* [80] also observed this same unexplained blue-shift in their THG measurements.

To understand the spectral and temporal information in Figure 5, we examine transients at fixed probe frequencies and spectra at fixed time delays in Figure 6. For both cases, we use simple models to ensure standard physical arguments can explain our observations. The specifics of the spectral lineshape model (results shown as solid lines in Figure 6a and Figure 6b) are discussed in Appendix C.

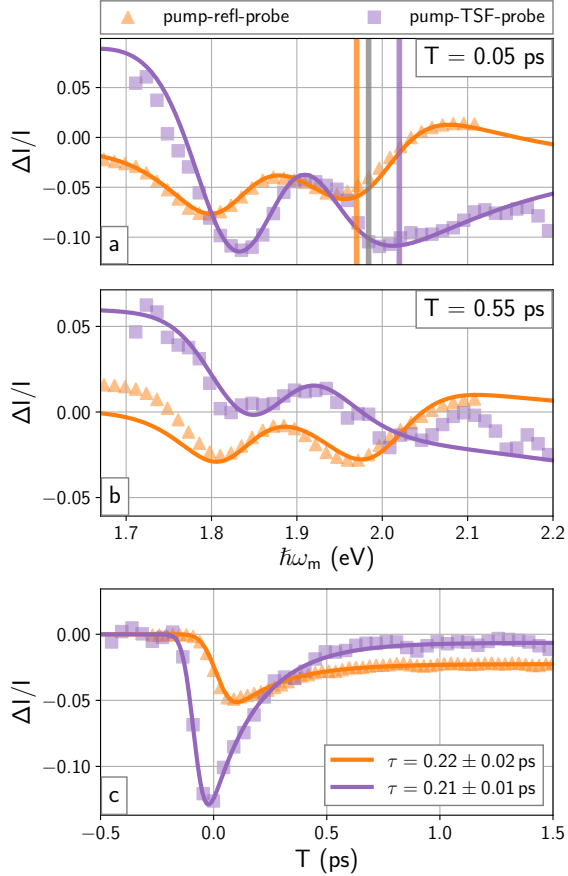


FIG. 6. Comparison of spectral and temporal lineshapes with $\hbar\omega_{\text{pump}} = 1.98$ eV (gray vertical line). Spectral lineshapes in (a) and (b) are acquired with delay times of 0.05 and 0.55 ps, respectively. Dynamics in (c) are acquired at probe energies indicated by the vertical lines in (a) (1.97 and 2.02 eV for pump-refl-probe and pump-TSF-probe, respectively). Solid lines in each plot are calculated from the models described in the main text and Appendix C.

We first consider the spectral slices. In both spectroscopies, the lineshape at $T \approx 0$ (Figure 6a) can be explained by a ~ 10 meV redshift, slight broadening, and slight amplitude decreases of the A and B resonances. Appendix C details the parameters used to generate the solid lines in Figure 6a and Figure 6b. A short time after excitation, $T = 0.55$ ps, the spectra are defined by a few meV redshift, no broadening, and no amplitude

decrease. In order to describe the pump-TSF-probe lineshape in Figure 6b we incorporated an additional ESA background. We attribute the additional ESA to excitation of near band edge carriers (conduction band electrons, valence band holes, or excitons) upon pump photoexcitation and subsequent relaxation. We attribute the redshift to carrier-induced bandgap renormalization (BGR), which was previously predicted and observed by many in monolayer TMDCs).[8, 81–84] The lineshape broadening upon excitation is common in semiconductors and has been previously observed by refs. [85, 86] in TMDCs. The amplitude decrease is likely due to state/band filling, in this simple model, we cannot distinguish between changes in transition density and transition dipole.

Dynamics were described by an exponential decay and a static offset:

$$\frac{\Delta I}{I}(T) = \left(A_0 \exp\left(-\frac{T}{\tau}\right) + A_1 \right) \Theta(T - t_0), \quad (17)$$

in which Θ is the Heaviside step function. We convolve Equation 17 with an instrument response function, which we approximate as Gaussian. Results are shown as solid lines in Figure 6c). Both spectroscopies exhibit time constants of ~ 200 fs (Table I).[87] Dynamics on this timescale have previously been attributed to several mechanisms, including carrier trapping,[88–90] carrier-carrier scattering,[85, 91] carrier-phonon scattering,[92–94] free-carrier screening effects,[86, 95] and exciton formation.[95] The longer dynamic in Figure 6c, which we treat as an offset, A_1 , has been observed by others.[89, 95]

TABLE I. Results from fitting Equation 17 to the dynamics shown in Figure 6b. FWHM = full width at half maximum of the instrument response function.

	pump-refl-probe	pump-TSF-probe
$\hbar\omega_m$ (eV)	1.97	2.02
τ (ps)	0.22 ± 0.02	0.21 ± 0.01
FWHM (ps)	0.125 ± 0.009	0.095 ± 0.006

Figure 7 shows the response from both TR and transient-THG spectroscopies for different combinations of pump and probe frequencies when $T = 50$ fs. Figure 7a is a very similar measurement to refs. [45, 96–102] where “traditional” coherent multidimensional spectroscopies were accomplished on TMDCs using a single electric field interaction as a probe; this measurement similarity is not the case for Figure 7b in which TSF acts as the probe with three electric field interactions. Nevertheless, both of our spectroscopies in Figure 7 have a similar dependence on the pump frequency—this can be seen by comparing vertical slices of Figure 7a and b (these horizontal slices are analogous to horizontal slices of Figure 5).[103] The lineshapes of our two spectroscopies change smoothly as a function of $\hbar\omega_{\text{pump}}$ —there are no distinct contributions from the A or B resonances along

the pump axis. The lack of structure along the pump axis mirrors the results of transient grating measurements on a MoS₂ thin film.[45] The general insensitivity to pump color suggests band gap renormalization (BGR) is a large contributor to the pump-induced changes. BGR is determined by Coulomb interactions, which are less sensitive to the explicit electron and hole occupation than, for instance, Pauli blocking effects.

Conversely, small, but noticeable, dependencies on ω_{pump} suggest secondary contributions to the TR and transient-TSF spectra. For instance, when $\hbar\omega_{\text{pump}} \approx 1.8 \text{ eV} \approx \hbar\omega_A$, the decreases in intensity at $\omega_{\text{out}} = \omega_A$, are $\sim 15\%$ larger than at $\omega_{\text{out}} = \omega_B$ for both TR and pump-TSF-probe. When $\hbar\omega_{\text{pump}} \approx \hbar\omega_B$, however, both A and B have similar decreases in intensity. We believe band/state filling (bleaching) can account for the observed asymmetries in the decreases in intensity. The MoS₂ valence band is energetically split for different hole spins, but the conduction band is energetically degenerate for electron spins (cf. inset in Figure 1). The A transition and B transition share neither valence nor conduction bands, so state/band filling is not shared between transitions. When the pump is resonant with the A transition, the bleach of the B transition is not direct and is expected to be smaller, in agreement with our measurements. Some bleaching is allowed through intervalley scattering, but valley depolarization measurements suggest these timescales are much longer than our pump probe delay time (50 fs) and is thus not significant.[104–106] When the pump is resonant with the B transition, it will also directly excite hot excitons or free electrons/holes from the A band, which explains why the effects on the A and B transitions are similar for these pump colors.

Guo *et al.* [102] also found asymmetries in the cross peaks of their multidimensional spectra of monolayer MoS₂ at 40 K. They attribute the asymmetric cross-peaks and their dynamics to be due to an exchange interaction between A and B excitons. This effect does not explain our results because the exchange interaction requires simultaneous populations of A and B excitons, which is not the case for $\omega_{\text{pump}} \approx \omega_A$.

C. MoS₂ and WS₂ nanostructures

In this section we investigate the effects of sample morphology on pump-TSF-probe spectroscopy by comparing all the samples shown in Figure 3. We first compare spectra of the previously discussed thin film with an ensemble of spiral nanostructures grown via a screw dislocation driven growth method (Figure 3b). The goal of this comparison is to broadly demonstrate that the spectra and dynamics observed with transient-TSF are sensitive to the specifics of sample morphology. We then compare the transient-TSF and TR response of both a WS₂ thin film and a single WS₂ screw-dislocation nanostructure.

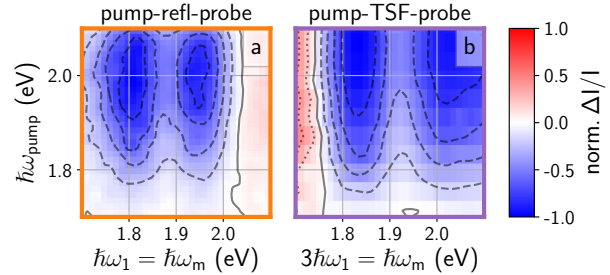


FIG. 7. Comparison between transient-reflectance spectroscopy (a) and transient-TSF spectroscopy (b) of a MoS₂ thin film. In both frames $T = 50$ fs.

1. Transient-THG of a MoS₂ thin film vs. nanostructures

Figure 8 shows the probe frequency vs. delay time response of the thin film (Figure 8a) and nanostructure (Figure 8b). Both spectra show similar spectral lineshapes near zero delay with decreases at the A and B features. The nanostructures spectrum (Figure 8b) demonstrate narrower peaks and greater increase in TSF intensity to the red of the A exciton resonance compared to the thin film (Figure 8a). The nanostructures exhibiting narrower features indicates that the thin film has more structural inhomogeneity. While both samples show similar lineshapes at $T = 0$, they exhibit drastically different dynamics.

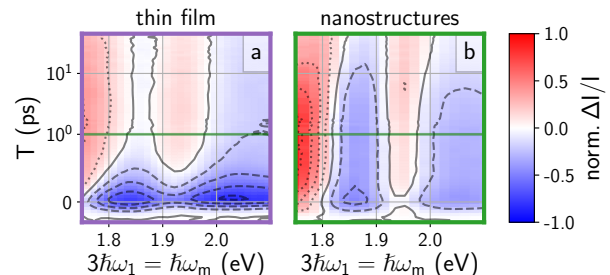


FIG. 8. Pump-TSF-probe spectra of a MoS₂ thin film (a) and a MoS₂ spiral nanostructure ensemble (b). The temporal axis has linear scaling until 1 ps (green line) and then logarithmic scaling until the end (50 ps). In both frames $\hbar\omega_{\text{pump}} = 3.1 \text{ eV}$ with a fluence of $120 \mu\text{J}/\text{cm}^2$.

Figure 9 shows a single temporal trace through the data shown in Figure 8 for each sample morphology. The thin lines are the measured data and the thick lines are fits using Equation 17. We recover exponential decay time constants of 0.34 ± 0.02 ps for the thin film and

12.7 ± 0.8 ps for the nanostructures. The morphology strongly affects dynamics. It is likely the case that the dramatic differences in timescales are related to the density of grain boundaries, which can affect carrier scattering, recombination, and/or trapping. The grain size of the thin film is on the order of 100 nm^2 while that of the nanostructures is on the order of $10\text{-}100 \mu\text{m}^2$. We believe that carrier trapping is the main source of dynamics in Figure 9; a carrier once it has been trapped is not able to efficiently screen the electron-hole Coulomb interaction, so BGR is lessened and the observed differential response is decreased.

There is a low amplitude, rapid dynamic present for each sample in Figure 9 that is not captured by our single exponential fit; we attribute this rapid dynamic to hot carriers (the carriers have ~ 1 eV excess energy upon photoexcitation) cooling to form excitons.[86, 95] In TMDCs, hot carriers bleach excitonic transitions more effectively than excitons; so a hot carrier cooling will reduce the bleach observed at the A and B transitions.[86, 95, 107] Taken together, we believe defect/grain-boundary assisted quenching of carriers along with hot carrier cooling can explain the dynamics observed in Figure 8 and Figure 9.

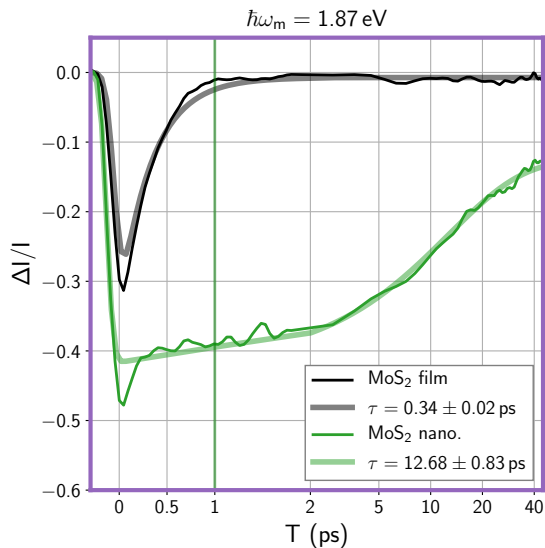


FIG. 9. Pump-TSF-probe of a MoS_2 thin film and an ensemble of spiral nanostructures. The temporal axis has linear scaling until 1 ps (green line) and then logarithmic scaling until the end (50 ps). This figure displays 1D slices out of Figure 8 in which the pump is set to $\hbar\omega_{\text{pump}} = 3.1$ eV while the probe is set to $3\hbar\omega_1 = \hbar\omega_m = 1.87$ eV.

2. Transient-THG vs. transient-reflectance for WS_2 thin film vs. single nanostructure

To further investigate the abilities of pump-TSF-probe, we performed pump-TSF-probe and pump-reflectance-probe experiments on two different morphologies of WS_2 : a thin film on a fused silica substrate (photo shown in Figure 3a), and a single, isolated, spiral nanostructure grown on a 300 nm SiO_2 on Si substrate (optical microscope and atomic force microscope characterization shown in Figure 3c, and Figure 3b, respectively). Our probe beam area is small compared to the area of the thin film, but much larger than the single nanostructure.

In Figure 10 we use a NIR pump to drive mid-gap or 2-photon transitions and probe the A exciton transition of WS_2 . Appendix D describes experiments on our MoS_2 thin film which demonstrate our ability to drive mid-gap transitions with a NIR pump. The full spectra and a discussion of these NIR pump measurements will be the subject of another publication. The unpumped THG spectra of the thin film and nanostructure are shown in Figure 10a, and the differential spectra ($T = 120$ fs) for each morphology are shown in Figure 10b. In both cases, the thin film exhibits a broader and redder A feature than the nanostructure—structural inhomogeneity from the small grain size of the polycrystalline film likely causes the increased linewidth of the thin film. The differing amount of spectral inhomogeneity causes the transient-reflectance and transient-TSF spectra between the two samples to look slightly different.

While we are able to measure clean transient-TSF spectra from both the thin film and single nanostructure, the same is less true for transient-reflectance measurements. Figure 10c shows that in addition to the qualitative differences in lineshape compared to the film, the nanostructure transient-reflectance signal is barely resolvable above measurement noise—it is at least 5 times weaker than the film’s response. Comparing the noise levels (width of the lines) between the two methods (Figure 10b and c) shows that pump-TSF-probe maintains a much higher signal-to-noise ratio than pump-reflectance-probe. This sensitivity is due to the stronger scaling of TSF to transition dipole (Equation 4, μ^8) compared to reflectance (μ^2). Since TMDC excitons interact strongly with light, the TSF emission from the substrates (fused silica and silicon) is negligible compared to the direct emission from the nanostructure. In contrast, reflectance measurements are heavily dependent on the substrate and its refractive index (Equation 9). As a result, TSF and pump-TSF-probe spectroscopies are insensitive to surface coverage and substrate layering, but reflectance and pump-reflectance-probe are sensitive to these effects.

V. OUTLOOK AND CONCLUSION

This work shows that pump-TSF-probe spectroscopy can elucidate the dynamics and energetics of photoex-

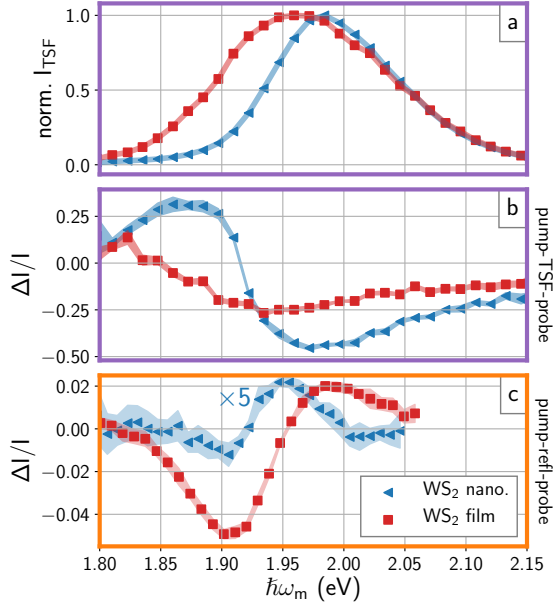


FIG. 10. Comparison of pump-TSF-probe and pump-reflectance-probe for two morphologies of WS_2 : a thin film and a single, $\sim 150 \mu\text{m}$ wide spiral nanostructure. (a) normalized TSF spectrum for each sample, these spectra are not normalized for the frequency dependent intensity of the probe OPA. (b) pump-TSF-probe spectra for each sample. (c) pump-refl-probe spectra for each sample. In (b) and (c) the non-resonant pump has frequency of $\hbar\omega_{\text{pump}} = 1.054 \text{ eV}$ and a fluence of $\sim 7000 \mu\text{J}/\text{cm}^2$. All spectra were acquired for the same number of laser shots. Each spectra is composed of 7 spectra averaged together at $T \approx 0.12 \text{ ps}$. (b) and (c) each show the standard deviation of the averaged spectra for each sample morphology as a filled spread around the average.

cited semiconductor thin films and nanostructures using the examples of MoS_2 and WS_2 . We demonstrated that this new spectroscopy (specifically the degenerate case of pump-TSF-probe, pump-THG-probe) and a more mature spectroscopy, transient-reflectance, can be understood in tandem from the same underlying physics. We found that transient-TSF is robust to extrinsic nanocrystal properties, such as size and surface coverage, that dramatically affect transient-reflectance spectra. This ro-

business allowed us to measure the transient-TSF spectrum of nanostructures much smaller than the excitation spot size, while at the same time maintaining a high signal-to-noise ratio. We predict that with pump-TSF-probe spectroscopy, researchers can avoid the reflectance artifacts which have complicated recent ultrafast work (cf. refs [108, 109]) because the measured TSF and pump-TSF-probe intensities are easily connected to the samples susceptibility.

Previous studies have shown that TSF can be used to measure coupling between states.[21, 28] Isolating cross peaks is a strategy not explored in this work that could further increase the selectivity of pump-TSF-probe spectroscopy in the future. We believe that samples with states/bands of the correct symmetry would yield insightful dynamical coupling information. For instance, since TSF can measure the energy separations of up to four states, it could resolve how bands change their dispersion upon photo-excitation.

Another area that could benefit from the proof-of-concept measurements in this work is multi-photon microscopy. Multiphoton microscopy uses a diverse set of techniques, including THG/TSF,[110–112] to predominantly measure biologically relevant samples. These multiphoton microscopies could easily incorporate a pump and a delay stage in order to measure spatially resolved dynamics.

SUPPLEMENTARY MATERIAL

All data and the workup/representation/simulation scripts used to generate the figures in this work are available for download at <http://dx.doi.org/10.17605/OSF.IO/UMSXC>.

ACKNOWLEDGMENTS

We acknowledge support from the Department of Energy, Office of Basic Energy Sciences, Division of Materials Sciences and Engineering, under award DE-FG02-09ER46664. D.J.M. acknowledges support from the Link Foundation. We thank Kyle Czech for synthesizing the MoS_2 thin film sample. D.J.M., D.D.K., and J.C.W. have filed a patent application on some of the work described herein.

Appendix A: Calculation of single resonance pump-THG-probe response

The single resonance third order susceptibility is given by

$$\chi^{(3)} = \frac{\mu^4}{\omega_{ag} - \omega_{321} - i\Gamma}. \quad (\text{A1})$$

We desire to calculate each term present in the total derivative

$$d\chi^{(3)} = \frac{\partial\chi^{(3)}}{\partial\mu}d\mu + \frac{\partial\chi^{(3)}}{\partial\omega_{ag}}d\omega_{ag} + \frac{\partial\chi^{(3)}}{\partial\Gamma}d\Gamma. \quad (\text{A2})$$

By taking derivatives of Equation A1 we find

$$\frac{\partial\chi^{(3)}}{\partial\mu}d\mu = \frac{4\mu^3d\mu}{\omega_{ag} - \omega_{321} - i\Gamma} \quad (\text{A3})$$

$$\frac{\partial\chi^{(3)}}{\partial\omega_{ag}}d\omega_{ag} = -\frac{\mu^4d\omega_{ag}}{(\omega_{ag} - \omega_{321} - i\Gamma)^2} \quad (\text{A4})$$

$$\frac{\partial\chi^{(3)}}{\partial\Gamma}d\Gamma = \frac{i\mu^4d\omega_{ag}}{(\omega_{ag} - \omega_{321} - i\Gamma)^2}. \quad (\text{A5})$$

We now desire to calculate $\frac{\Delta I}{I}$

$$\frac{\Delta I}{I} = \frac{|\chi^{(3)} + d\chi^{(3)}|^2 - |\chi^{(3)}|^2}{|\chi^{(3)}|^2} \quad (\text{A6})$$

$$= \left| 1 + \frac{d\chi^{(3)}}{\chi^{(3)}} \right|^2 - 1 \quad (\text{A7})$$

in which we have used the relationship $\frac{|a|}{|b|} = \left| \frac{a}{b} \right|$ for $b \neq 0$. Full substitution of Equation A1 and Equation A2 into Equation A7 yields a large equation which is too complicated to parse. A much simpler approach is to consider the limits of having only one of $\{d\mu, d\omega_{ag}, d\Gamma\}$ being nonzero at a time

$$\frac{\Delta I}{I} = 8\frac{d\mu}{\mu} + 16\left(\frac{d\mu}{\mu}\right)^2 \quad d\mu \neq 0 \quad (\text{A8})$$

$$\frac{\Delta I}{I} = \frac{d\Gamma}{(\omega_{ag} - \omega_{321})^2 + \Gamma^2} \left[-2\Gamma + \frac{d\Gamma}{(\omega_{ag} - \omega_{321})^2 + \Gamma^2} (\omega_{ag}^2 + \omega_{321}^2 + \Gamma^2 - 2\omega_{ag}\omega_{321}\Gamma) \right] \quad d\Gamma \neq 0 \quad (\text{A9})$$

$$\frac{\Delta I}{I} = \frac{d\omega_{ag}}{(\omega_{ag} - \omega_{321})^2 + \Gamma^2} \left[-2\omega_{ag} + 2\omega_{321} + \frac{d\omega_{ag}}{(\omega_{ag} - \omega_{321})^2 + \Gamma^2} (\omega_{ag}^2 + \omega_{321}^2 + \Gamma^2 - 2\omega_{ag}\omega_{321}) \right] \quad d\omega_{ag} \neq 0. \quad (\text{A10})$$

In the limit of small perturbation we may consider merely terms which are linear in all differentials

$$\frac{\Delta I}{I} \approx 8\frac{d\mu}{\mu} \quad d\mu \neq 0 \quad (\text{A11})$$

$$\frac{\Delta I}{I} \approx \frac{-2\Gamma d\Gamma}{(\omega_{ag} - \omega_{321})^2 + \Gamma^2} \quad d\Gamma \neq 0 \quad (\text{A12})$$

$$\frac{\Delta I}{I} \approx \frac{2d\omega_{ag}(\omega_{321} - \omega_{ag})}{(\omega_{ag} - \omega_{321})^2 + \Gamma^2} \quad d\omega_{ag} \neq 0. \quad (\text{A13})$$

This is the desired result which was discussed in the main text. The lineshape for $d\mu \neq 0$ corresponds to a uniform change in the spectrum. The lineshape for $d\Gamma \neq 0$ corresponds to the imaginary component of the original Lorentzian lineshape. The lineshape for $d\omega_{ag} \neq 0$ corresponds to the first derivative lineshape of the original Lorentzian.

Appendix B: Calculation of single resonance transient-transmittance response

We desire to calculate the transient-transmittance response expected for a sample with a single resonance such that

$$\chi^{(1)} = \frac{\mu^2}{\omega_{ag} - \omega_1 - i\Gamma}. \quad (\text{B1})$$

If we assume our samples are thick enough for Beer's law to apply, then the total amount of light with original intensity of I_0 transmitted through a sample of length ℓ is given by

$$T = I_0 \exp(-\alpha\ell) \quad (\text{B2})$$

with $\alpha = \frac{2\pi \text{Im}[\chi^{(1)}]}{\lambda_1 n} = \frac{\omega_1 \text{Im}[\chi^{(1)}]}{cn}$. The transient-transmittance (absorbance) response can be constructed as

$$\frac{\Delta T}{T} = \frac{T_{\text{pumped}} - T_{\text{unpumped}}}{T_{\text{unpumped}}} \quad (\text{B3})$$

$$= \frac{I_0 \exp(-\alpha_{\text{pumped}}\ell) - I_0 \exp(-\alpha_{\text{unpumped}}\ell)}{I_0 \exp(-\alpha_{\text{unpumped}}\ell)} \quad (\text{B4})$$

$$= \exp(\alpha_{\text{unpumped}}\ell - \alpha_{\text{pumped}}\ell) - 1. \quad (\text{B5})$$

Taylor expansion using $\exp(x) = 1 + x + \dots$ yields

$$\frac{\Delta T}{T} \approx \ell (\alpha_{\text{unpumped}} - \alpha_{\text{pumped}}). \quad (\text{B6})$$

We now let $\alpha = \frac{\omega_1 \text{Im}[\chi^{(1)}]}{cn}$ and $\chi_{\text{pumped}}^{(1)} = \chi_{\text{unpumped}}^{(1)} + d\chi^{(1)}$ which yields

$$\frac{\Delta T}{T} \approx \ell \left(\frac{\omega_1 \text{Im}[\chi_{\text{unpumped}}^{(1)}]}{cn} - \frac{\omega_1 \text{Im}[\chi_{\text{unpumped}}^{(1)} + d\chi^{(1)}]}{cn} \right) \quad (\text{B7})$$

$$= -\frac{\omega_1 \ell}{cn} \text{Im}[d\chi^{(1)}]. \quad (\text{B8})$$

In the case of small perturbation, $d\chi^{(1)}$ may be described by the total derivative

$$d\chi^{(1)} = \frac{\partial \chi^{(1)}}{\partial \mu} d\mu + \frac{\partial \chi^{(1)}}{\partial \omega_{ag}} d\omega_{ag} + \frac{\partial \chi^{(1)}}{\partial \Gamma} d\Gamma. \quad (\text{B9})$$

Each type of change ($d\mu$, $d\omega_{ag}$, $d\Gamma$) affects the observed lineshape of $\frac{\Delta T}{T}$. We consider the cases where only one of the differentials is non-zero at a time. The partial derivatives and imaginary projects are trivial and the results are

$$\frac{\Delta T}{T} = -\left(\frac{\omega_1 \ell}{cn}\right) \frac{2\mu \Gamma d\mu}{(\omega_{ag} - \omega_1)^2 + \Gamma^2} \quad d\mu \neq 0 \quad (\text{B10})$$

$$\frac{\Delta T}{T} = -\left(\frac{\omega_1 \ell}{cn}\right) \frac{2\mu^2 \left((\omega_{ag} - \omega_1)^2 - \Gamma^2\right) d\Gamma}{\left((\omega_{ag} - \omega_1)^2 + \Gamma^2\right)^2} \quad d\Gamma \neq 0 \quad (\text{B11})$$

$$\frac{\Delta T}{T} = \left(\frac{\omega_1 \ell}{cn}\right) \frac{2\mu^2 \Gamma (\omega_{ag} - \omega_1) d\omega_{ag}}{\left((\omega_{ag} - \omega_1)^2 + \Gamma^2\right)^2} \quad d\omega_{ag} \neq 0. \quad (\text{B12})$$

The lineshape for $d\mu \neq 0$ corresponds to the imaginary component of the original Lorentzian lineshape. The lineshape for $d\Gamma \neq 0$ corresponds to the second derivative lineshape of the original Lorentzian. The lineshape for $d\omega_{ag} \neq 0$ corresponds to the first derivative lineshape of the original Lorentzian.

Appendix C: Lineshape modeling

In this appendix we describe our simple model for building the spectral lineshapes shown in Figure 6. The general implementation is:

1. For both spectroscopies construct an unexcited $\chi^{(n)}$ spectrum from a sum of oscillators.
2. Calculate the unexcited reflectance or TSF spectrum from $\chi^{(1)}$ and $\chi^{(3)}$, respectively.
3. Create a $\chi^{(n)'$ spectrum to perturb the central frequencies, linewidths, and amplitudes of the oscillators used to construct $\chi^{(n)}$.

4. Calculate the excited reflectance or TSF spectrum from $\chi^{(1)'}$ and $\chi^{(3)'}$, respectively.
5. Use Equation 12 to calculate $\frac{\Delta I}{I}$ for both spectroscopies.
6. Iterate through previous steps to fit observed lineshapes.

We choose to use complex, Lorentzian oscillators to construct our spectra:

$$\chi^{(n)} = \sum_{j=1} \sqrt{\frac{\Gamma_j}{\pi}} \frac{A_j}{E_{0,j} - \hbar\omega_m - i\Gamma_j} \quad (\text{C1})$$

in which $j = 1$ and $j = 2$ are the A and B transitions, and the other oscillators are high-lying non-resonant transitions. To create $\chi^{(n)'}$ we replace $\Gamma_j \rightarrow \Gamma_j + \Delta\Gamma_j$, $E_{0,j} \rightarrow E_{0,j} + \Delta E_{0,j}$, and $A_j \rightarrow (1 - \% \text{ decrease})A_j$. ESA-like additional transitions are incorporated by adding a phased offset to $\chi^{(n)'}$; the pump-TSF-probe spectrum in Figure 6b has a slight offset with phase described by $\exp[i\theta]$ with $\theta = 1$ radian. Table II codifies the parameters we found, by hand, to give acceptable fits to the data shown in Figure 6.

We construct a TSF spectrum by merely calculating the square magnitude of $\chi^{(3)}$ as indicated by Equation 10. We construct a reflectance spectrum by converting $\chi^{(1)}$ to a complex refractive index, \bar{n} and then using a Fresnel-coefficient-like analysis, specifically as discussed in Anders [113], which takes into account the influence of multiple reflections and the substrate. This treatment is slightly more holistic than merely using Equation 5 because it takes into account the finite thickness of the sample (while the derivation of Equation 5 assumes a delta function sample). R is calculated using

$$R = \left| \frac{\bar{r}_1 + \bar{r}_2 \exp[-i\phi_1]}{1 + \bar{r}_1 \bar{r}_2 \exp[-i\phi_1]} \right|^2 \quad (\text{C2})$$

$$\bar{r}_1 = \frac{\bar{n}_0 - \bar{n}_1}{\bar{n}_0 + \bar{n}_1} \quad (\text{C3})$$

$$\bar{r}_2 = \frac{\bar{n}_1 - \bar{n}_2}{\bar{n}_1 + \bar{n}_2} \quad (\text{C4})$$

$$\phi_1 = \frac{4\pi\ell\bar{n}_1}{\lambda} \quad (\text{C5})$$

in which \bar{n}_0 is the refractive index of air, \bar{n}_1 is the constructed refractive index of the MoS₂ thin film with thickness ℓ , \bar{n}_2 is the refractive index of the fused silica substrate, and λ is the vacuum wavelength of the interrogating electric field.

TABLE II. Parameters used to produce the lineshapes shown in Figure 6. Note that the model in Figure 6b for pump-TSF-probe has a slight offset with phase described by $\exp[i\theta]$ with $\theta = 1$ radian and amplitude of 1% of the maximum feature.

transition	E_0 (eV)	ΔE_0 (eV)	Γ (eV)	$\Delta\Gamma$ (eV)	relative A	% A decrease
transient reflectance model $T = 0.05$ ps						
A	1.807	-0.01	0.1	0.002	1	2
B	1.98	-0.009	0.12	0.005	1.1	2
	2.7	-0.008	0.25	0	4	5
	3.2	0	0.25	0	8	0
	6	0	0.25	0	40	0
transient reflectance model $T = 0.55$ ps						
A	1.807	-0.005	0.1	0.002	1	2
B	1.98	-0.005	0.12	0.005	1.1	2
	2.7	0	0.25	0	4	5
	3.2	0	0.25	0	8	0
	6	0	0.25	0	40	0
transient TSF model $T = 0.05$ ps						
A	1.81	-0.012	0.085	0.005	1	2
B	1.95	-0.009	0.1	0.005	0.91	2
transient TSF model $T = 0.55$ ps						
A	1.81	-0.003	0.085	0	1	0
B	1.95	-0.002	0.1	0	0.91	0

Appendix D: Transient-reflectance with NIR excitation of a MoS₂ thin film

TMCDs are known to be weakly absorptive well below bandgap (c.f. Bikorimana *et al.* [114]). To investigate this sub-band edge response, we tuned our pump to NIR colors, using fluence an order of magnitude higher than the visible pump. The effects of this sub-band edge pump on the band-edge reflectance spectrum are shown in Figure 11. We observe similar spectral and temporal lineshapes for both the visible and NIR pump, indicating the NIR pump generates photocarriers in a similar manner to a visible pump.

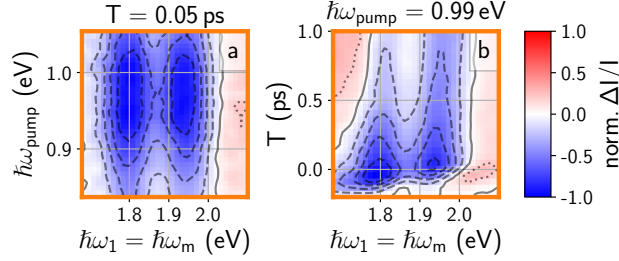


FIG. 11. Transient-reflectance spectroscopy on a MoS₂ thin film with a NIR pump. (a) shows the transient-reflectance spectrum for different combinations of pump and probe frequencies for $T = 50$ fs. Note that this spectrum is not normalized for the setpoint frequency dependence of the pump laser intensity. (b) shows the measured dynamics for different probe colors with $\hbar\omega_{\text{pump}} = 0.99$ eV

Given the strong two-photon absorption in TMDCs,[115–119] it is reasonable to attribute the signals in Figure 11 to two-photon absorption from the pump. We find, however, that the TR and pump-THG-probe scale linearly or sublinearly, rather than quadratically, with pump fluence (Figure 12). Furthermore, pump-induced reflectance responses occur with pump photon energies below half the band edge. These observations rule out two-photon absorption as the dominant contribution to Figure 11.

We conclude that our NIR pump excites electrons/holes to/from midgap states which have small optical cross-sections. Midgap states are known to exist in synthetically grown MoS₂ and are generally attributed to sulfur vacancies and edge defects.[88, 120–125] We believe mid-gap excitations can induce BGR and band-filling in a manner similar to direct, allowed transitions, which explains the similarity between visible and NIR pumps (compare Figure 7 a with Figure 11a or Figure 5a with Figure 11b). The insensitivity to pump wavelength reflects the large dispersion of mid-gap states and their transitions to valence and conduction bands.

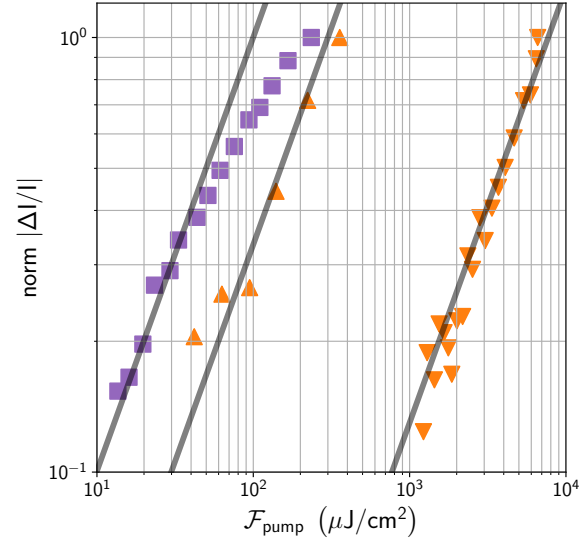


FIG. 12. Comparison of transient-reflectance spectroscopy (orange) to transient-TSF spectroscopy (violet) pump fluence scaling for a MoS₂ thin film. The y-axis is maximum extent of the bleach measured (near $T = 0$). The pump and probe combinations are as follows: (▲, $\hbar\omega_1 = \hbar\omega_m = \hbar\omega_{\text{pump}} = 1.98$ eV); (▼, $\hbar\omega_1 = \hbar\omega_m = 1.98$ eV, $\hbar\omega_{\text{pump}} = 0.99$ eV); and (■, $3\hbar\omega_1 = \hbar\omega_m = 2.05$ eV, $\hbar\omega_{\text{pump}} = 1.98$ eV). Gray lines are guides to the eye signifying linear scaling of response with pump fluence.

-
- [1] R. Ulbricht, E. Hendry, J. Shan, T. F. Heinz, and M. Bonn, *Reviews of Modern Physics* **83**, 543 (2011).
- [2] W. Xiong, J. E. Laaser, P. Paoprasert, R. A. Franking, R. J. Hamers, P. Gopalan, and M. T. Zanni, *Journal of the American Chemical Society* **131**, 18040 (2009).
- [3] D. R. Dietze and R. A. Mathies, *ChemPhysChem* **17**, 1224 (2016).
- [4] A. E. Bragg, W. Yu, J. Zhou, and T. Magnanelli, *The Journal of Physical Chemistry Letters* **7**, 3990 (2016).
- [5] F. Ceballos, M.-G. Ju, S. D. Lane, X. C. Zeng, and H. Zhao, *Nano Letters* **17**, 1623 (2017).
- [6] A. Mandal, J. D. Schultz, Y.-L. Wu, A. F. Coleman, R. M. Young, and M. R. Wasielewski, *The Journal of Physical Chemistry Letters*, 3509 (2019).
- [7] E. J. Sie, C. M. Nyby, C. D. Pemmaraju, S. J. Park, X. Shen, J. Yang, M. C. Hoffmann, B. K. Ofori-Okai, R. Li, A. H. Reid, S. Weathersby, E. Mannebach, N. Finney, D. Rhodes, D. Chenet, A. Antony, L. Balicas, J. Hone, T. P. Devereaux, T. F. Heinz, X. Wang, and A. M. Lindenberg, *Nature* **565**, 61 (2019).
- [8] F. Liu, M. E. Ziffer, K. R. Hansen, J. Wang, and X. Zhu, *Physical Review Letters* **122** (2019), 10.1103/physrevlett.122.246803.
- [9] F. Langer, C. P. Schmid, S. Schlauderer, M. Gmitra, J. Fabian, P. Nagler, C. Schüller, T. Korn, P. G. Hawkins, J. T. Steiner, U. Huttner, S. W. Koch, M. Kira, and R. Huber, *Nature* **557**, 76 (2018).
- [10] Z. Wang, H. Park, Y. H. Lai, J. Xu, C. I. Blaga, F. Yang, P. Agostini, and L. F. DiMauro, *Nature Communications* **8** (2017), 10.1038/s41467-017-01899-1.
- [11] J. C. Wright, *Annual Review of Physical Chemistry* **62**, 209 (2011).
- [12] J. C. Wright, *Annual Review of Analytical Chemistry* **10**, 45 (2017).
- [13] P. C. Chen, *Applied Spectroscopy* **70**, 1937 (2016).
- [14] C. L. Smallwood and S. T. Cundiff, *Laser & Photonics Reviews* **12**, 1800171 (2018).
- [15] S. T. Cundiff and S. Mukamel, *Physics Today* **66**, 44 (2013).
- [16] M. Cho, *Chemical Reviews* **108**, 1331 (2008).
- [17] M. Cho, ed., *Coherent Multidimensional Spectroscopy* (Springer Singapore, 2019).
- [18] J. Bredenbeck, J. Helbing, R. Behrendt, C. Renner, L. Moroder, J. Wachtveitl, and P. Hamm, *The Journal of Physical Chemistry B* **107**, 8654 (2003).
- [19] B. Abraham, L. G. C. Rego, and L. Gundlach, *The Journal of Physical Chemistry C* (2019), 10.1021/acs.jpcc.9b03849.
- [20] N. A. Neff-Mallon and J. C. Wright, *Analytical Chemistry* **89**, 13182 (2017).
- [21] J. D. Handali, K. F. Sunden, B. J. Thompson, N. A. Neff-Mallon, E. M. Kaufman, T. C. Brunold, and J. C. Wright, *The Journal of Physical Chemistry A* **122**, 9031 (2018).
- [22] E. S. Boyle, A. V. Pakoulev, and J. C. Wright, *The Journal of Physical Chemistry A* **117**, 5578 (2013).
- [23] E. S. Boyle, N. A. Neff-Mallon, and J. C. Wright, *The Journal of Physical Chemistry A* **117**, 12401 (2013).
- [24] E. S. Boyle, N. A. Neff-Mallon, J. D. Handali, and J. C. Wright, *The Journal of Physical Chemistry A* **118**, 3112 (2014).
- [25] M. Grechko, T. Hasegawa, F. D'Angelo, H. Ito, D. Turchinovich, Y. Nagata, and M. Bonn, *Nature Communications* **9** (2018), 10.1038/s41467-018-03303-y.
- [26] M. Bonn, C. Hess, J. H. Miners, T. F. Heinz, H. J. Bakker, and M. Cho, *Physical Review Letters* **86**, 1566 (2001).
- [27] D. J. Morrow, D. D. Kohler, K. J. Czech, and J. C. Wright, *The Journal of Chemical Physics* **149**, 091101 (2018).
- [28] M. Grechko, S. A. Bretschneider, L. Vietze, H. Kim, and M. Bonn, *Angewandte Chemie International Edition* **57**, 13657 (2018).
- [29] K. F. Mak, C. Lee, J. Hone, J. Shan, and T. F. Heinz, *Physical Review Letters* **105** (2010), 10.1103/physrevlett.105.136805.
- [30] G. Wang, A. Chernikov, M. M. Glazov, T. F. Heinz, X. Marie, T. Amand, and B. Urbaszek, *Reviews of Modern Physics* **90** (2018), 10.1103/revmodphys.90.021001.
- [31] A. Molina-Sánchez, D. Sangalli, K. Hummer, A. Marini, and L. Wirtz, *Physical Review B* **88** (2013), 10.1103/physrevb.88.045412.
- [32] D. Y. Qiu, F. H. da Jornada, and S. G. Louie, *Physical Review Letters* **111** (2013), 10.1103/physrevlett.111.216805.
- [33] K. He, N. Kumar, L. Zhao, Z. Wang, K. F. Mak, H. Zhao, and J. Shan, *Physical Review Letters* **113** (2014), 10.1103/physrevlett.113.026803.
- [34] N. Saigal, V. Sugunakar, and S. Ghosh, *Applied Physics Letters* **108**, 132105 (2016).
- [35] J. Kopaczek, M. P. Polak, P. Scharoch, K. Wu, B. Chen, S. Tongay, and R. Kudrawiec, *Journal of Applied Physics* **119**, 235705 (2016).
- [36] A. Autere, H. Jussila, Y. Dai, Y. Wang, H. Lipsanen, and Z. Sun, *Advanced Materials* **30**, 1705963 (2018).
- [37] Y. M. Chang, L. Xu, and H. W. K. Tom, *Physical Review Letters* **78**, 4649 (1997).
- [38] C. Guo, G. Rodriguez, and A. J. Taylor, *Physical Review Letters* **86**, 1638 (2001).
- [39] A. McClelland, V. Fomenko, and E. Borguet, *The Journal of Physical Chemistry B* **108**, 3789 (2004).
- [40] D. Hsieh, F. Mahmood, J. W. McIver, D. R. Gardner, Y. S. Lee, and N. Gedik, *Physical Review Letters* **107** (2011), 10.1103/physrevlett.107.077401.
- [41] W. A. Tisdale, K. J. Williams, B. A. Timp, D. J. Norris, E. S. Aydil, and X.-Y. Zhu, *Science* **328**, 1543 (2010).
- [42] H. Park, M. Gutierrez, X. Wu, W. Kim, and X.-Y. Zhu, *The Journal of Physical Chemistry C* **117**, 10974 (2013).
- [43] C. A. Nelson, J. Luo, A. K.-Y. Jen, R. B. Laghumavarapu, D. L. Huffaker, and X.-Y. Zhu, *The Journal of Physical Chemistry C* **118**, 27981 (2014).
- [44] E. M. Mannebach, K.-A. N. Duerloo, L. A. Pellouchoud, M.-J. Sher, S. Nah, Y.-H. Kuo, Y. Yu, A. F. Marshall, L. Cao, E. J. Reed, and A. M. Lindenberg, *ACS Nano* **8**, 10734 (2014).
- [45] K. J. Czech, B. J. Thompson, S. Kain, Q. Ding, M. J. Shearer, R. J. Hamers, S. Jin, and J. C. Wright, *ACS Nano* **9**, 12146 (2015).
- [46] J. P. Lomont, K. L. Rich, M. Maj, J.-J. Ho, J. S. Ostran-

- der, and M. T. Zanni, *The Journal of Physical Chemistry B* **122**, 144 (2017).
- [47] A. M. Alperstein, J. S. Ostrander, T. O. Zhang, and M. T. Zanni, *Proceedings of the National Academy of Sciences* **116**, 6602 (2019).
- [48] A. Taghizadeh and T. G. Pedersen, *Phys. Rev. B* **99**, 235433 (2019).
- [49] A. Taghizadeh and T. G. Pedersen, *Phys. Rev. B* **97**, 205432 (2018).
- [50] A. Taghizadeh, F. Hipolito, and T. G. Pedersen, *Phys. Rev. B* **96**, 195413 (2017).
- [51] T. G. Pedersen, *Phys. Rev. B* **92**, 235432 (2015).
- [52] D. B. S. Soh, C. Rogers, D. J. Gray, E. Chatterjee, and H. Mabuchi, *Phys. Rev. B* **97**, 165111 (2018).
- [53] R. W. Boyd, *Nonlinear Optics*, 3rd ed. (Academic Press, 2008).
- [54] N. Bloembergen and Y. R. Shen, *Physical Review* **133**, A37 (1964).
- [55] L. A. Falkovsky, *J. Phys. Conf. Ser.* **129**, 012004 (2008).
- [56] E. J. Sie, A. J. Frenzel, Y.-H. Lee, J. Kong, and N. Gedik, *Physical Review B* **92** (2015), 10.1103/physrevb.92.125417.
- [57] TSF emission from the substrate is also possible, but in practice this contribution is negligible compared to TMDC thin films when measuring in the reflective direction c.f. the SI of Morrow *et al.* [27].
- [58] N. Bloembergen and P. S. Pershan, *Physical Review* **128**, 606 (1962).
- [59] A crucial filter for our TSF probe experiments is a 1000 nm longpass filter (ThorLabs FGL1000M) which ensures no visible light from secondary OPA processes reach the sample. Notably, double polished silicon was not a suitable filter because it created non-negligible THG as well as lossy transmission.
- [60] K. Furuta, M. Fuyuki, and A. Wada, *Applied Spectroscopy* **66**, 1475 (2012).
- [61] D. J. Morrow, D. D. Kohler, and J. C. Wright, *Physical Review A* **96** (2017), 10.1103/physreva.96.063835.
- [62] J. D. Handali, K. F. Sunden, E. M. Kaufman, and J. C. Wright, *Chemical Physics* (2018), 10.1016/j.chemphys.2018.05.023.
- [63] D. J. Morrow, *Open Science Framework* (2019), 10.17605/OSF.IO/UMSXC.
- [64] B. J. Thompson, K. F. Sunden, D. J. Morrow, and N. A. Neff-Mallon, “PyCMDS,” (2018).
- [65] B. Thompson, K. Sunden, D. Morrow, D. Kohler, and J. Wright, *Journal of Open Source Software* **4**, 1141 (2019).
- [66] E. Jones, T. Oliphant, and P. Peterson, “SciPy: Open source scientific tools for Python,” (2001), [Online; accessed 2017-09-28].
- [67] S. van der Walt, S. C. Colbert, and G. Varoquaux, *Computing in Science & Engineering* **13**, 22 (2011).
- [68] J. D. Hunter, *Computing in Science & Engineering* **9**, 90 (2007).
- [69] Y. Zhao and S. Jin, “Controllable water vapor assisted chemical vapor transport synthesis of WS₂-MoS₂ heterostructure,” (2019), arXiv:1909.01390.
- [70] C. Lee, H. Yan, L. E. Brus, T. F. Heinz, J. Hone, and S. Ryu, *ACS Nano* **4**, 2695 (2010).
- [71] H. Li, Q. Zhang, C. C. R. Yap, B. K. Tay, T. H. T. Edwin, A. Olivier, and D. Baillargeat, *Advanced Functional Materials* **22**, 1385 (2012).
- [72] A. Berkdemir, H. R. Gutiérrez, A. R. Botello-Méndez, N. Perea-López, A. L. Elías, C.-I. Chia, B. Wang, V. H. Crespi, F. López-Urías, J.-C. Charlier, H. Terrones, and M. Terrones, *Scientific Reports* **3**, 1755 EP (2013), article.
- [73] M. J. Shearer, L. Samad, Y. Zhang, Y. Zhao, A. Puzos, K. W. Eliceiri, J. C. Wright, R. J. Hamers, and S. Jin, *Journal of the American Chemical Society* **139**, 3496 (2017).
- [74] X. Fan, Y. Zhao, W. Zheng, H. Li, X. Wu, X. Hu, X. Zhang, X. Zhu, Q. Zhang, X. Wang, B. Yang, J. Chen, S. Jin, and A. Pan, *Nano Letters* **18**, 3885 (2018).
- [75] X. Fan, Y. Jiang, X. Zhuang, H. Liu, T. Xu, W. Zheng, P. Fan, H. Li, X. Wu, X. Zhu, Q. Zhang, H. Zhou, W. Hu, X. Wang, L. Sun, X. Duan, and A. Pan, *ACS Nano* **11**, 4892 (2017).
- [76] L. Zhang, K. Liu, A. B. Wong, J. Kim, X. Hong, C. Liu, T. Cao, S. G. Louie, F. Wang, and P. Yang, *Nano Letters* **14**, 6418 (2014).
- [77] H. Zhang, Y. Wan, Y. Ma, W. Wang, Y. Wang, and L. Dai, *Applied Physics Letters* **107**, 101904 (2015).
- [78] M. M. Benameur, B. Radisavljevic, J. S. Héron, S. Sahoo, H. Berger, and A. Kis, *Nanotechnology* **22**, 125706 (2011).
- [79] P. Blake, E. W. Hill, A. H. Castro Neto, K. S. Novoselov, D. Jiang, R. Yang, T. J. Booth, and A. K. Geim, *Applied Physics Letters* **91**, 063124 (2007), <https://doi.org/10.1063/1.2768624>.
- [80] R. Wang, H.-C. Chien, J. Kumar, N. Kumar, H.-Y. Chiu, and H. Zhao, *ACS Applied Materials & Interfaces* **6**, 314 (2013).
- [81] E. A. A. Pogna, M. Marsili, D. D. Fazio, S. D. Conte, C. Manzoni, D. Sangalli, D. Yoon, A. Lombardo, A. C. Ferrari, A. Marini, G. Cerullo, and D. Prezzi, *ACS Nano* **10**, 1182 (2016).
- [82] A. Chernikov, C. Ruppert, H. M. Hill, A. F. Rigosi, and T. F. Heinz, *Nature Photonics* **9**, 466 (2015).
- [83] A. Steinhoff, M. Rösner, F. Jahnke, T. O. Wehling, and C. Gies, *Nano Letters* **14**, 3743 (2014).
- [84] L. Meckbach, T. Stroucken, and S. W. Koch, *Applied Physics Letters* **112**, 061104 (2018).
- [85] S. Sim, J. Park, J.-G. Song, C. In, Y.-S. Lee, H. Kim, and H. Choi, *Physical Review B* **88** (2013), 10.1103/physrevb.88.075434.
- [86] P. D. Cunningham, A. T. Hanbicki, K. M. McCreary, and B. T. Jonker, *ACS Nano* **11**, 12601 (2017).
- [87] Because these lineshapes are not merely caused by amplitude changes (J or μ), fitting different probe colors results in different decay rates, with τ up to 0.4 ps.
- [88] P. D. Cunningham, K. M. McCreary, A. T. Hanbicki, M. Currie, B. T. Jonker, and L. M. Hayden, *The Journal of Physical Chemistry C* **120**, 5819 (2016).
- [89] H. Shi, R. Yan, S. Bertolazzi, J. Brivio, B. Gao, A. Kis, D. Jena, H. G. Xing, and L. Huang, *ACS Nano* **7**, 1072 (2013).
- [90] P. Schietecatte, P. Geiregat, and Z. Hens, *The Journal of Physical Chemistry C* **123**, 10571 (2019).
- [91] D. Tsokkou, X. Yu, K. Sivula, and N. Banerji, *The Journal of Physical Chemistry C* **120**, 23286 (2016).
- [92] Z. Nie, R. Long, L. Sun, C.-C. Huang, J. Zhang, Q. Xiong, D. W. Hewak, Z. Shen, O. V. Prezhdo, and Z.-H. Loh, *ACS Nano* **8**, 10931 (2014).
- [93] N. Kumar, J. He, D. He, Y. Wang, and H. Zhao, *Journal of Applied Physics* **113**, 133702 (2013).

- [94] Z. Nie, R. Long, J. S. Teguh, C.-C. Huang, D. W. Hewak, E. K. L. Yeow, Z. Shen, O. V. Prezhdo, and Z.-H. Loh, *The Journal of Physical Chemistry C* **119**, 20698 (2015).
- [95] F. Ceballos, Q. Cui, M. Z. Bellus, and H. Zhao, *Nanoscale* **8**, 11681 (2016).
- [96] A. Singh, G. Moody, S. Wu, Y. Wu, N. J. Ghimire, J. Yan, D. G. Mandrus, X. Xu, and X. Li, *Physical Review Letters* **112** (2014), 10.1103/physrevlett.112.216804.
- [97] G. Moody, C. K. Dass, K. Hao, C.-H. Chen, L.-J. Li, A. Singh, K. Tran, G. Clark, X. Xu, G. Berghäuser, E. Malic, A. Knorr, and X. Li, *Nature Communications* **6** (2015), 10.1038/ncomms9315.
- [98] A. Singh, G. Moody, K. Tran, M. E. Scott, V. Overbeck, G. Berghäuser, J. Schaibley, E. J. Seifert, D. Pleskot, N. M. Gabor, J. Yan, D. G. Mandrus, M. Richter, E. Malic, X. Xu, and X. Li, *Physical Review B* **93** (2016), 10.1103/physrevb.93.041401.
- [99] K. Hao, G. Moody, F. Wu, C. K. Dass, L. Xu, C.-H. Chen, L. Sun, M.-Y. Li, L.-J. Li, A. H. MacDonald, and X. Li, *Nature Physics* **12**, 677 (2016).
- [100] K. Hao, L. Xu, P. Nagler, A. Singh, K. Tran, C. K. Dass, C. Schüller, T. Korn, X. Li, and G. Moody, *Nano Letters* **16**, 5109 (2016).
- [101] K. Hao, J. F. Specht, P. Nagler, L. Xu, K. Tran, A. Singh, C. K. Dass, C. Schüller, T. Korn, M. Richter, A. Knorr, X. Li, and G. Moody, *Nature Communications* **8** (2017), 10.1038/ncomms15552.
- [102] L. Guo, M. Wu, T. Cao, D. M. Monahan, Y.-H. Lee, S. G. Louie, and G. R. Fleming, *Nature Physics* **15**, 228 (2018).
- [103] The decrease in $\Delta I/I$ at high pump frequencies in the TR experiment Figure 7a is likely caused by a decrease in the I_{pump} at those frequencies. The two spectra in Figure 7 were collected at different times and do not share the same pump intensity spectrum.
- [104] F. Mahmood, Z. Alpichshev, Y.-H. Lee, J. Kong, and N. Gedik, *Nano Letters* **18**, 223 (2017).
- [105] L. Yang, N. A. Sinitsyn, W. Chen, J. Yuan, J. Zhang, J. Lou, and S. A. Crooker, *Nature Physics* **11**, 830 (2015).
- [106] G. Moody, J. Schaibley, and X. Xu, *Journal of the Optical Society of America B* **33**, C39 (2016).
- [107] S. Schmitt-Rink, D. S. Chemla, and D. A. B. Miller, *Physical Review B* **32**, 6601 (1985).
- [108] J. Liu, J. Leng, S. Wang, J. Zhang, and S. Jin, *The Journal of Physical Chemistry Letters* **10**, 97 (2019).
- [109] T. Ghosh, S. Aharon, A. Shpatz, L. Etgar, and S. Ruhman, *ACS Nano* **12**, 5719 (2018).
- [110] A. M. Hanninen, R. C. Prince, and E. Potma, *IEEE Journal of Selected Topics in Quantum Electronics* , 1 (2018).
- [111] A. M. Hanninen, R. C. Prince, R. Ramos, M. V. Plikus, and E. O. Potma, *Biomedical Optics Express* **9**, 4807 (2018).
- [112] H. Segawa, M. Okuno, H. Kano, P. Leproux, V. Couderc, and H. o Hamaguchi, *Optics Express* **20**, 9551 (2012).
- [113] H. Anders, *Thin Films in Optics* (The Focal Press, 1967).
- [114] S. Bikorimana, P. Lama, A. Walser, R. Dorsinville, S. Anghel, A. Mitioglu, A. Micu, and L. Kulyuk, *Optics Express* **24**, 20685 (2016).
- [115] S. Zhang, N. Dong, N. McEvoy, M. O'Brien, S. Winters, N. C. Berner, C. Yim, Y. Li, X. Zhang, Z. Chen, L. Zhang, G. S. Duesberg, and J. Wang, *ACS Nano* **9**, 7142 (2015).
- [116] Z. Ye, T. Cao, K. O'Brien, H. Zhu, X. Yin, Y. Wang, S. G. Louie, and X. Zhang, *Nature* **513**, 214 (2014).
- [117] T. C. Berkelbach, M. S. Hybertsen, and D. R. Reichman, *Physical Review B* **92** (2015), 10.1103/physrevb.92.085413.
- [118] N. Dong, Y. Li, S. Zhang, N. McEvoy, R. Gatensby, G. S. Duesberg, and J. Wang, *ACS Photonics* **5**, 1558 (2018).
- [119] Q. Cui, Y. Li, J. Chang, H. Zhao, and C. Xu, *Laser & Photonics Reviews* **13**, 1800225 (2018).
- [120] A. M. van der Zande, P. Y. Huang, D. A. Chenet, T. C. Berkelbach, Y. You, G.-H. Lee, T. F. Heinz, D. R. Reichman, D. A. Muller, and J. C. Hone, *Nature Materials* **12**, 554 (2013).
- [121] W. Zhou, X. Zou, S. Najmaei, Z. Liu, Y. Shi, J. Kong, J. Lou, P. M. Ajayan, B. I. Yakobson, and J.-C. Idrobo, *Nano Letters* **13**, 2615 (2013).
- [122] Z. G. Yu, Y.-W. Zhang, and B. I. Yakobson, *Nano Letters* **15**, 6855 (2015).
- [123] J. Hong, Z. Hu, M. Probert, K. Li, D. Lv, X. Yang, L. Gu, N. Mao, Q. Feng, L. Xie, J. Zhang, D. Wu, Z. Zhang, C. Jin, W. Ji, X. Zhang, J. Yuan, and Z. Zhang, *Nature Communications* **6** (2015), 10.1038/ncomms7293.
- [124] H. Qiu, T. Xu, Z. Wang, W. Ren, H. Nan, Z. Ni, Q. Chen, S. Yuan, F. Miao, F. Song, G. Long, Y. Shi, L. Sun, J. Wang, and X. Wang, *Nature Communications* **4** (2013), 10.1038/ncomms3642.
- [125] C.-P. Lu, G. Li, J. Mao, L.-M. Wang, and E. Y. Andrei, *Nano Letters* **14**, 4628 (2014).